Journal of civil engineering and transport **transEngin**

2020, Volume **2** Number **3** **ISSN 2658-1698, e-ISSN 2658-2120**

DOI: 10.24136/tren.2020.009

WAVELET METHOD OF EDGE DETECTION IN IMAGES WITH HIGH-NOISE LEVEL

Tadeusz **Niedziela** [1]

[1] University of Technology and Humanities, Faculty of Transport, Electrical Engineering and Computer Science, Malczewskiego 29, 26-600 Radom, Poland, t.niedziela@uthrad.pl, https://orcid.org/0000-0002-4772-3797

Reviewed positively: 28.02.2020

Information about quoting an article:

Niedziela T. (2020). Wavelet method of edge detection in images with high-noise level. Journal of civil engineering and transport. 2(3), 119-130, ISSN 2658-1698, e-ISSN 2658-2120, DOI: 10.24136/tren.2020.009

Abstract – In the paper a mathematical model addressed to non-sharp edges in the images is proposed. This model is based on and integral transform with Haar-Gauss wavelet and matching algorithm of bandwidth, such model is used to detection of the edges in images with high-level noises, both in the x plane and the frequency domains. There is shown that applying the integral Haar-Gaussian transformation the detection of single and double edges is possible. Demonstrated in the paper results confirm that wavelet transform supported by the matching wavelet algorithm of wavelength bandwidth make an important exploration tool of the images with the edges possessing a large depth of sharpness.

Key words – characteristic features, detection of non-sharp edges, Haar-Gauss wavelet, wavelet transforms

JEL Classification – C29, C95, C96

INTRODUCTION

Images obtained naturally or artificially always contain characteristic areas. Physical parameters such as brightness, luminance or chromaticity change slowly inside the highlighted area, but change extremely quickly between the areas that create the edges. The edge is a transition between different areas and often carries interesting physical information. In image processing, edge detection is the basis of many applications such as object recognition in transport vision systems, automated observation, automatic control, biomedical imaging, electro-optical measurements, etc. Measuring systems are often based on optical imaging. Objects can be measured at different distances from the imaging system. This generates two problems. The first problem is the different magnifications for objects at different distances that can make a significant measurement error. The second problem is the imaging system has limited depth of field (DOF). Inside the depth of field, the image is sharp enough, but outside the depth of field (focus), the edges in the image become non-sharp, which is known as the lack of focus effect. When measuring a large object, the two problems mentioned above become important. In addition, the imposed noise worsens the results.

Edge detection is currently most often carried out using integral digital methods. If the image is not noisy, then these methods give good results. However, for blurry images, edge detection using digital integral methods can be affected by significant errors. To overcome the second problem related to depth of field, wavelet transforms [1-8] have recently been proposed for detecting noisy edges. The results are more accurate and adapt better than standard digital integral methods.

The purpose of this article is to propose an integral wavelet transform for the detection of non-sharp edges implemented in intelligent vision transport systems, whose mother wavelet is the Haar-Gauss function. A wavelet of this type proposed for edge detection can be used both in x space and in the frequency domain ν. The bandwidth matching algorithm is used to achieve high precision edge detection.

1. MATHEMATICAL MODEL OF EDGE FUNCTION

An ideal image of a straight edge $\eta(x)$ (geometric function of an ideal edge) (Fig. 1a) can be described by the equation (1):

$$\eta(x) = a(1 - 2\int_{-\infty}^{\infty} \delta(\varsigma)d(\varsigma) = -a\,\mathrm{sgn}\begin{pmatrix} a & x < 0 \\ -a & x \geq 0 \end{pmatrix} \tag{1}$$

where: sgn(x) – character function.

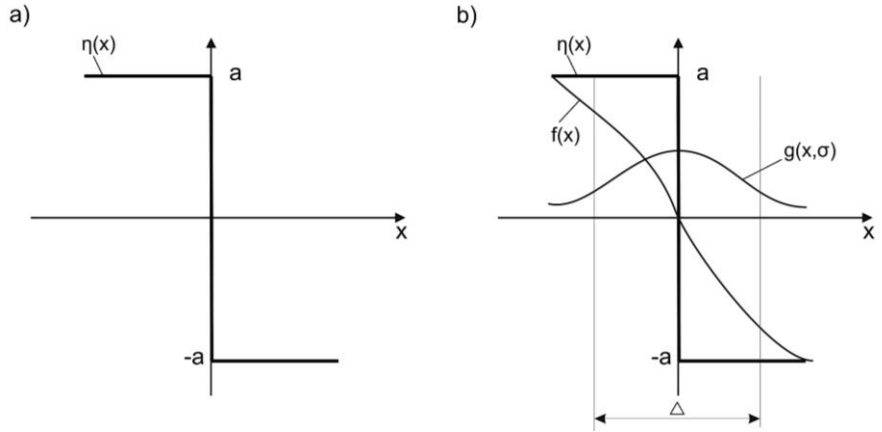

Fig. 1. Model of an ideal edge η(x): a) model of real edge f(x), b) model of span index g(x) with the geometric edge function η(x)

In simplification, the ideal image of a straight edge η(x) is called the geometric function of a straight edge.

The real edge image f(x) is a transition zone, not a geometric straight edge, and is most often uniformly variable. Moreover, the real edge image is the edge function f(x) described by (2). Mathematically, the edge function f(x) can be described as a convolution of the function of the span index g(x) and the geometric edge function η(x).

$$f(x) = g(x) \otimes \eta(x) \tag{2}$$

The function of span index g(x) contains all factors that allow to creating a real edge image. Naturally, the function of span index is most often a Gaussian function (3):

$$g(x,\sigma) = \exp\left[-\left(\frac{x}{\sigma}\right)^2\right] \tag{3}$$

For example, vibrations make the image of a straight edge a slow-changing transition zone. Substituting equations (1) and (3) to (2) a function describing the real edge is obtained (4):

$$\begin{aligned} f(x) = g(x) \otimes \eta(x) &= \frac{a}{\sigma\sqrt{\pi}}\int_{-\infty}^{\infty} g(\xi,\sigma)\cdot \mathrm{sgn}(x-\varsigma)d\zeta) = \\ &= \frac{a}{\sigma\sqrt{\pi}}\int_{-\infty}^{\infty} \exp\left[-\left(\frac{\xi}{\sigma}\right)^2\right]\cdot \mathrm{sgn}(x-\varsigma)d\zeta = \frac{a}{\sigma\sqrt{\pi}}\int_{-\infty}^{\infty} \exp\left[-\left(\frac{\xi}{\sigma}\right)^2\right]d\zeta = a\,\mathrm{erf}\left[\frac{x}{\sigma}\right] \end{aligned} \tag{4}$$

where: erf(x) – function of error.

Standardized parameters ensure convergence f(x) to ±a for x —» ±∞. For the purposes of analysis, equivalent edge width ΔS is defined as a derivative of the function of the actual edge f(x). The derivative of the function k (4) at x=0 has the form (5).

$$\begin{aligned} k_0 = k\,|_{x=0} = -\frac{df(x)}{dx}\,|_{x=0} &= -\frac{a}{\sigma\sqrt{\pi}}\left\{\int_{-\infty}^{\infty} g(\xi,\sigma)\cdot\frac{\vartheta[\mathrm{sgn}(x-\varsigma)]}{\vartheta x}\cdot d\zeta\right\}_{x=0} = \\ &= \frac{2a}{\sigma\sqrt{\pi}}\left\{\int_{-\infty}^{\infty} g(\xi,\sigma)\cdot\delta(x-\varsigma)\cdot d\zeta\right\}_{x=0} = \frac{2a}{\sigma\sqrt{\pi}} \end{aligned} \tag{5}$$

Accordingly, the equivalent edge width takes the form (6):

$$\Delta S = \frac{2a}{k_0} = \sigma\sqrt{\pi} = 1{,}77\sigma \tag{6}$$

which can be determined by function of span index g(x, σ) of edge function f(x). The function of span index g(x, σ) and equivalent edge width ΔS are shown on the Figure 1b.

By using the properties of the Fourier transform, the bandwidth ΔW in the frequency domain ν for the edge function f(x) is described as (7) and is understood as the uncertainty factor (UF):

$$\Delta W = \frac{1}{\Delta S} = \frac{1}{\sqrt{\pi\sigma}} = \frac{k_0}{2a} \tag{7}$$

The small ΔS and wide ΔW describe the sharp edge, which means that more high frequency components are contained in f(x). Conversely, if the object has more non-sharp edges (large ΔS), the narrower its bandwidth ΔW is. In practical edge detection, this means that different object structures (i.e. different edge locations) have different frequency bandwidths for the same edge. Specifying, different functions of the span index g give different edge widths ΔS. In addition, the image can be heavily noisy, which has hitherto prevented the use of standard integral digital methods for detecting non-sharp (noisy) edges.

2. HAAR-GAUSS INTEGRAL WAVELET TRANSFORM

For the detection of non-sharp edges, an integral wavelet transform with the Haar-Gauss wavelet $h_s(x)$ is proposed (8).

$$h_s(x) = \frac{2}{s}\left(\frac{x-q}{s}\right)\cdot\exp\left[-\left(\frac{x-q}{s}\right)^2\right] - \frac{2}{s}\left(\frac{x+q}{s}\right)\cdot\exp\left[-\left(\frac{x+q}{s}\right)^2\right] \tag{8}$$

where: s - positive scaling parameter, q - extending parameter.
Figures 2a and 2b illustrate Haar-Gauss wavelets $h_s(x)$ for large and small expansion parameters (q=5s and q=2.5s).

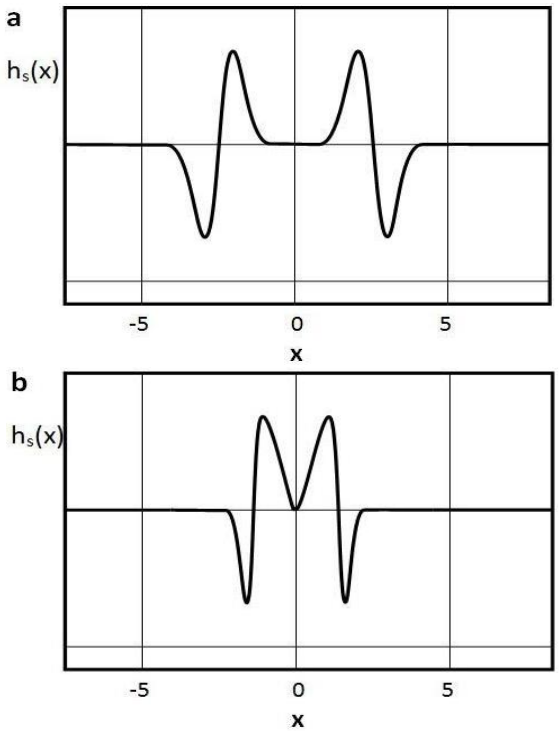

Fig. 2. Haar-Gauss wavelet $h_s(x)$ for q=5s (a) and for q=2,5s (b)

When the extending parameter q approaches the scaling parameter s, then both peaks of Haar-Gauss wavelet approach each other. Finally, when q=s, the double-peak wavelet goes into a single-peak wavelet (Fig. 3a), resembles a "Mexican hat" wavelet. The double-peak wavelet can be useful for detecting (detecting) single and double edges. At first this article proposes the detection of a single edge using a single-peak wavelet (q=s) shown in Fig. 3a. Although, the Haar-Gaussian wavelet for q=s is not exactly the same as the "Mexican hat" wavelet, however, both functions share common features - a single peak with two side humps as shown in Fig. 3a.

The Haar-Gauss integral wavelet transform W{g(x)} of the g(x) signal in space x is defined as (9):

$$W\{g(x)\} = \int_{-\infty}^{\infty} h_s\left[\left(\frac{\xi - x}{s}\right)\right] \cdot g(\xi) d\zeta \qquad (9)$$

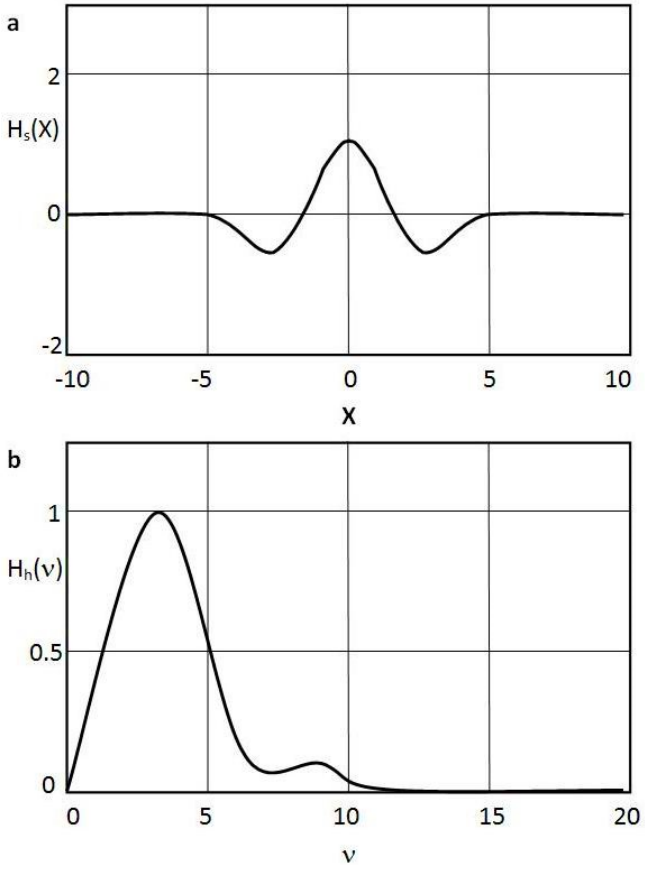

Fig. 3. Haar-Gauss wavelet $h_s(x)$ for q=s (a) and Fourier spectrum $H_h(\nu)$ (b)

Correspondingly, the Haar-Gauss integral wavelet transform (H-G) in the frequency domain W{g(ν)} (in Fourier space) is defined as (10):

$$W\{g(\nu)\} = \int_{-\infty}^{\infty} H(\nu) \cdot G(\nu) \cdot \exp(i2\pi\nu)\, d\nu \qquad (10)$$

where: H(ν) i G(ν) – respectively Fourier transforms of Haar-Gauss wavelet and g(x) signal.

The H-G wavelet is illustrated in both *x* space (Fig. 3a) and ν frequency space (Fig. 3b). Equation (10) indicates that the H-G wavelet transform behaves like a filter. Its non-zero area becomes a wavelet frequency window. The width of the spatial Haar-Gauss wavelet window ΔS_h is described by (11):

$$\Delta S_h = 2s\left[\frac{\left(h(x), x^2, h(x)\right)}{\left(h(x), h(x)\right)}\right]^{\frac{1}{2}} = 2s\left[\frac{\int_{-\infty}^{\infty} x^2 \cdot [h(x)]^2 dx}{\int_{-\infty}^{\infty} [h(x)]^2 dx}\right]^{\frac{1}{2}} \quad (11)$$

Substituting the Haar-Gauss wavelet $h_s(x)$ (8) to (11), an equivalent edge width ΔS_h is obtained (12):

$$\Delta S_h = 2sq\left[\frac{\frac{3}{4q^2}\left(1-e^{-2q^2}\right)+1+e^{-2q^2}}{1-\left(1-4q^2\right)\cdot e^{-2q^2}}\right]^{\frac{1}{2}} \quad (12)$$

When the parameter extending the H-G wavelet is large (q»1), then the edge width ΔS_h in x space approximately is obtained (13).

$$\Delta S_h = 2sq \quad (13)$$

The Fourier transform of Haar-Gauss wavelet described (8) is (14):

$$H_h(\nu) = -s\nu \cdot \sin(2\pi sg\nu) \cdot e^{-(\pi s\nu)^2} \quad (14)$$

For q=s the Fourier transform of H-G wavelet is illustrated on Fig.3b. First maximum of $H_h(\nu)$ is approximately in point ν_c (15):

$$\nu_c = \frac{1}{4sq} \quad (15)$$

Thus ν_c can be considered as the center frequency of the Fourier spectrum of the Haar-Gauss wavelet. The window bandwidth ΔW_h in the mid-frequency domain is (16):

$$\Delta W_h = \frac{1}{2sq} \quad (16)$$

Then the curl factor is (17):

$$\Delta S_h \cdot \Delta W_h = 1 \quad (17)$$

The H-G wavelet transform is a smoothing procedure. The smaller is the width ΔS_h, the wider the frequency window ΔW_h. Accordingly, the set of collected frequencies is more resourceful. On the other hand, the noise band (especially white noise) is very wide, which means that more noise is collected when the frequency window expands (which increases the measurement error). The appropriate bandwidth for specific detection should be chosen. The ratio of the central frequency ν_c to the width of the window ΔW_h, is a parameter of measurement precision Q, and is equal to (18):

$$Q = \frac{\nu_c}{\Delta W_h} = \frac{1}{2} \quad (18)$$

The precision parameter Q is therefore independent of the center frequency. The frequency window expands as the central frequency increases. Because the measurement accuracy is proportional to Q, it means that using the H-G wavelet transform the same accuracy is obtained for different spatial frequencies.

For practical applications, the H-G wavelet transform can be considered as a filter in the frequency domain. The edge understood as part of the image has a limited number of frequency components. In practice, the filter width can be selected to be slightly wider than the edge spectrum bandwidth.

In this way, the basic frequency components of the signal will be collected, while the unnecessary components and noise will be filtered out. Consequently, the S/N ratio will increase and errors will decrease significantly.

According to the uncertainty principle, the edge bandwidth ΔW is directly proportional to the edge slope k_0. Therefore, the value of the edge width measurement could estimate by measuring k_0. Correct selection of the bandwidth ΔW of the H-G wavelet width window can both secure the measurement accuracy and also significantly save calculation time. The described selection method can be understood as a bandwidth matching algorithm.

The ratio of edge bandwidth ΔW_h to frequency bandwidth ΔW can be considered as a matching parameter β. By using equations (7) and (16) can obtain (19):

$$\beta = \frac{\Delta W_h}{\Delta W} = \frac{\Delta S}{\Delta S_h} = \frac{a}{qk_0} = \frac{\sqrt{\pi}\cdot\sigma}{2sq} \quad (19)$$

According to the band matching algorithm, the result sq of the H-G wavelet is determined by the bandwidth of the edge ΔW. The Haar-Gauss wavelet transform W{f(x)} of edge function f(x) is (20):

$$W\{f(x)\} = \int_{-\infty}^{\infty} H_h(\nu)\cdot F(\nu)\cdot \exp(i2\pi\nu)\, d\nu = \frac{2as}{\sqrt{s^2+\sigma^2}}\left[e^{-\left(\frac{x-x_0}{\sigma\mu}\right)^2} - e^{-\left(\frac{x+x_0}{\sigma\mu}\right)^2} \right] \tag{20}$$

where:

$$\mu = \sqrt{1+\frac{\pi}{4\beta^2 q^2}}; \quad x_0 = \frac{\sqrt{\pi}\cdot\sigma}{2\beta}$$

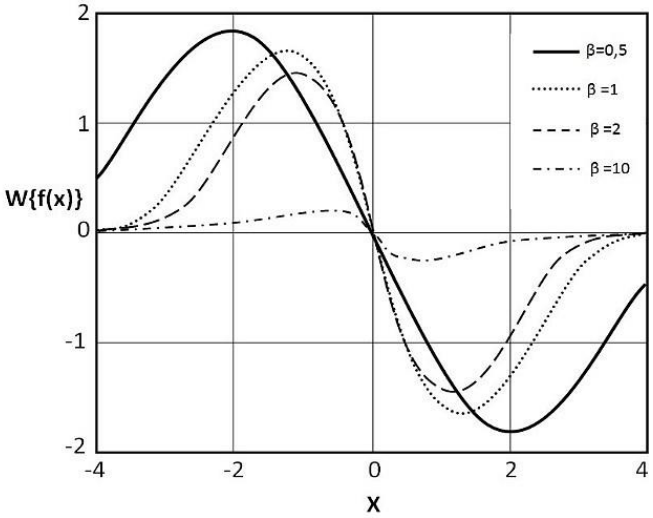

Fig. 4. Haar-Gauss integral wavelet transform W{f(x)} of edge function f(x) for chosen matching parameters β

Figure 4 illustrates the Haar-Gauss integral wavelet transform W{f(x)} of edge function f(x) (results of the (20) equation) for four cases of matching parameters $\beta = 0.5, 1, 2, 10$. It can be seen that the zero point indicates the geometry position of edge (Fig. 1a), which it means the central point of edge function f(x) (Fig. 1b).

3. CHARACTERISTIC FEATURES OF OBJECTS IN THE IMAGE SPACE

The contours of objects are very often used in image recognition using their characteristic features (both their shape factors as well as geometrical and central moments).

Among the many known shape factors, the group constituting the basic of traditional recognition methods can be mentioned. A popular designation for these methods is the use of the letter W along with the method number. The most popular shape factors are W1, W2, and W3. There are more advanced W5 or W6 factors that refer to complex features.

The two groups of characteristics presented above can be used together or only some factors can be selected, deciding either for a more accurate reproduction of the shape of objects or for faster operation of the algorithm.

Sometimes intermediate features are useful (W7, W8). These are: W7 coefficient, examining the variability of the minimum and maximum distance of the center of gravity from the contour of the object, and W8 coefficient giving the ratio of the maximum size to the perimeter of the object. The basic coefficients are presented in Table 1.

In most technical problems, where objects on the raster are large enough so that their shapes can be accurately evaluated - the values of these coefficients allow for convenient and reliable distinction of objects of different shapes. What's more, each of the discussed coefficients is a scalar measure of the described shape - calculating the values of these coefficients allows for a marginal reduction in the amount of information contained in the image. From tens of thousands of numbers describing the image in terms of pixels, the equivalent vector of characteristics features is created. Based on its value, the shape of the object can easily determine.

Table 1. Shape factors

circularity ratio	$W1 = 2\sqrt{\frac{S}{\pi}}$
circularity ratio	$W2 = \frac{L}{\pi}$
Malinowska's coefficient	$W3 = \frac{L}{2\sqrt{\pi S}} - 1$
Blair-Bliss's coefficient	$W4 = \frac{S}{\sqrt{2\pi\iint\left(r^2\right)ds}}$
Danielsson's coefficient	$W5 = \frac{S^3}{\left(\iint_S l ds\right)^2}$
Haralick's coefficient	$W6 = \sqrt{\frac{\left(\sum d\right)^2}{n\sum d^2 - 1}}$
Lp1 coefficient	$W7 = \frac{r_{min}}{R_{max}}$
Lp2 coefficient	$W8 = \frac{L_{max}}{L}$
Mz coefficient	$W9 = \frac{2\sqrt{\pi S}}{L}$

where:
L - object projection perimeter,
S - field of the object projection,
R - distance of the field element from the object's center of gravity,
l - minimum distance of element from the object's contour,
d - distance of the pixels of the object's contour from its center of gravity,
n - number of contour points,
r_{min} - minimum contour distance from the center of gravity,
R_{max} - maximum contour distance from the center of gravity,
L_{max} - maximum size of the object.

However, the operation of these coefficients is not perfect even for ideal geometric figures, because they often take similar values for different figures, have varying sensitivity to changes in the proportion of the figure, and they are prone to discretization errors in varying degrees.

GEOMETRICAL MOMENTS

The function f(x,y) means the intensity distribution in the image. Individual pixels are assigned values in accordance with the function value f(x,y), where x,y are the coordinates of the pixel.

In the general case, the two-dimensional moment p,q of the row calculated for a function f(x,y) is defined as (21):

$$m_{pq} = \int_{-\infty}^{\infty}\int_{-\infty}^{\infty} x^p y^q f(x,y)\,dxdy \tag{21}$$

where: x,y - pixel position, while its value is described by the function f(x,y).

For digital images, the function is (22):

$$m_{pq} = \sum_R x^p y^q \tag{22}$$

where: R - describes the area of the figure being examined.

The basic geometrical moments of the row m_{ik} are defined as (23):

$$m_{00} = \frac{1}{2}\sum_{k=1}^{N} y_k x_{k-1} - x_k y_{k-1}$$

$$m_{10} = \frac{1}{2}\sum_{k=1}^{N}\left\{\begin{array}{l}\frac{1}{2}\left(x_k + x_{k-1}\right)\left(y_k x_{k-1} - x_k y_{k-1}\right)\\ -\frac{1}{6}\left(y_k - y_{k-1}\right)\left(x_k^2 + x_k x_{k-1} + x_{k-1}^2\right)\end{array}\right\} \tag{23}$$

$$m_{11} = \frac{1}{3}\sum_{k=1}^{N}\left(y_{k-1} - x_k y_{k-1}\right)\left(2x_k y_k + x_{k-1} y_k + x_k y_{k-1} + 2x_{k-1} y_{k-1}\right)$$

$$m_{20} = \frac{1}{3}\sum_{k=1}^{N}\frac{1}{2}\left\{\frac{1}{2}\left(x_k y_{k-1} - x_k y_{k-1}\right)\left(x_k^2 + x_k x_{k-1} + x_{k-1}^2\right) - \frac{1}{4}\left(y_k - y_{k-1}\right)\left(x_k^3 + x_k^2 x_{k-1} + x_k x_{k-1}^2 + x_{k-1}^3\right)\right\}$$

There are a number of momentary invariants expressed in the form of simple polynomial functions operating on values of central moments. These invariants are characterized by invariance due to the transformation of rotation in the image plane, scale changes and shifts. The two most of typical transformations are invariants Φ_1 and Φ_7.

where:

$$\gamma = \frac{p+q}{2}$$

$$\varphi_1 = \eta_{20} + \eta_{02}$$

$$\varphi_2 = (\eta_{20} + \eta_{02})^2 + 4\eta_{11}^2$$

$$\varphi_3 = (\eta_{30} + 3\eta_{12})^2 + (3\eta_{21} - \eta_{03})^2$$

$$\varphi_4 = (\eta_{30} + \eta_{12})^2 + (\eta_{21} + \eta_{03})^2$$

$$\varphi_5 = (\eta_{30} - 3\eta_{12})(\eta_{30} + \eta_{12})\left[(\eta_{30} + \eta_{12})^2 - (3\eta_{21} - \eta_{03})^2\right] + \ldots$$
$$+ (3\eta_{21} - \eta_{03})(\eta_{21} + \eta_{03})\left[3(\eta_{30} - \eta_{12})^2 - (\eta_{21} + \eta_{03})^2\right]$$

$$\varphi_6 = (\eta_{20} - \eta_{02})\left[(\eta_{30} + \eta_{12})^2 - (\eta_{21} + \eta_{03})^2\right] + 4\eta_{11}(\eta_{30} + \eta_{12})(\eta_{21} + \eta_{03})$$

$$\varphi_7 = \eta_{20}\eta_{02} - \eta_{11}^2$$

$$\varphi_8 = \eta_{30}\eta_{12} + \eta_{21}\eta_{03} - \eta_{11}^2 - \eta_{21}^2$$

$$\varphi_9 = \eta_{20}(\eta_{21}\eta_{03} - \eta_{12}^2) - \eta_{02}(\eta_{30}\eta_{12} - \eta_{21}^2) - \eta_{11}(\eta_{30}\eta_{03} - \eta_{21}\eta_{12})$$

$$\varphi_{10} = (\eta_{30}\eta_{03} - \eta_{12}\eta_{21})^2 - 4(\eta_{30}\eta_{12} - \eta_{21}^2)\cdot(\eta_{03}\eta_{21} - \eta_{12})$$

All of the above parameters are invariant due to rotation, translation and the scale change of the object. Based on them, a feature vector is created that characterizes the uniquely recognized object.

OBJECT LOCALIZATION

The location of the object usually comes down to determining the coordinates of its center of gravity, which is a fairly simple procedure that can be performed in a very short time. The method of calculating the center of gravity and the orientation of objects in the image begins with the description of the contour lines of the considered object in the form of a set of coordinate pairs of subsequent contour points (x_1,y_1), (x_2,y_2), …, (x_n,y_n). Then the values of its above described geometric characteristics can search using numerical formulas in the form:

- Surface area (25):

$$F = \frac{1}{2}\sum_{k=1}^{n}(x_k - x_{k+1})(y_k + y_{k+1}) \tag{25}$$

- Static moments (26) and (27):

$$S_x = \frac{1}{6}\sum_{k=1}^{n}(x_k - x_{k+1})(y_k^2 + y_k y_{k+1} + y_{k+1}^2) \tag{26}$$

$$S_y = \frac{1}{6}\sum_{k=1}^{n}(y_k - y_{k+1})(x_k^2 + x_k x_{k+1} + x_{k+1}^2) \tag{27}$$

INVARIANTS AND NORMALIZED CENTRAL MOMENTS

The normalized central moments η_{pq} and invariants Φ are defined as (24):

$$\eta_{pq} = \frac{\mu_{pq}}{m_{00}^{\gamma+1}} \tag{24}$$

– Gravity factors (28):

$$x_0 = \frac{S_y}{F};\quad y_0 = \frac{S_x}{F} \tag{28}$$

A more complex task is to determine the orientation of the object separated in the image (considered as a flat figure). The solution of this task is possible, among others, using geometrical characteristics used in mechanics to describe the dynamics of a rigid material system. These are mainly calculated tensor elements (assuming that the object is a homogeneous flat figure D) as follows (29) and (30):

$$J_{x0} = J_x - Fy_0^2;\ J_{y0} = J_y - Fx_0^2 \tag{29}$$

$$J_{x0y0} = J_{xy} - Fx_0y_0 \tag{30}$$

The components are calculated as follows.

– Moment of inertia (31) and (32):

$$J_x = \frac{1}{12}\sum_{k=1}^{n}\left(x_k - x_{k+1}\right)\left(y_k^3 + y_k^2y_{k+1} + y_ky_{k+1}^2 + y_{k+1}^3\right) \tag{31}$$

$$J_y = \frac{1}{12}\sum_{k=1}^{n}\left(y_k - y_{k+1}\right)\left(x_k^3 + x_k^2x_{k+1} + x_kx_{k+1}^2 + x_{k+1}^3\right) \tag{32}$$

– Moment of deviation (33):

$$J_{xy} = \frac{1}{24}\sum_{k=1}^{n}\left(x_k - x_{k+1}\right)\left[x_k\left(3y_k^2 + y_{k+1}^2 + 2y_ky_{k+1}\right) + x_{k+1}\left(3y_k^2 + y_k^2 + 2y_ky_{k+1}\right)\right] \tag{33}$$

The coordinates of the center of gravity are calculated from (28).

Based on the above-mentioned parameters, further characteristics can be calculated. The main central moments of inertia (34):

$$\begin{aligned} J_{\xi 0} &= \frac{J_{x0} + J_{y0}}{2} + \frac{1}{2}\sqrt{\left(J_{y0} - J_{x0}\right)^2 + 4J_{x0y0}} \\ J_{\vartheta 0} &= \frac{J_{x0} + J_{y0}}{2} - \frac{1}{2}\sqrt{\left(J_{y0} - J_{x0}\right)^2 + 4J_{x0y0}} \end{aligned} \tag{34}$$

In order to find indicators determining the spatial orientation of the object, the directions of the main central inertia axes should be determined as (35):

$$\begin{aligned} \alpha_{\xi 0} &= \operatorname{arctg}\frac{J_{x0y0}}{J_{y0} - J_{\xi 0}} \\ \alpha_{\vartheta 0} &= \operatorname{arctg}\frac{J_{x0y0}}{J_{y0} - J_{\vartheta 0}} \end{aligned} \tag{35}$$

Knowing the angles given in (35), the orientations of the observed object, according to the axis of inertia of the solid can be determined.

4. RESULTS OF TESTS

Figure 5 shows the simulated function of the real edge f(x) in grayscale (dashed line) and its Haar-Gauss integral wavelet transform W{f(x)+B} (solid line). The Haar-Gauss wavelet transform is an integral W{f(x)+B} = W{f(x)}.

The Fourier spectrum of the edge function f(x) in grayscale and the spectrum of its wavelet transform H-G is illustrated by dashed and solid lines, respectively. The H-G wavelet bandwidth was taken as three times from the corresponding edge bandwidth ($\beta = 3$).

To obtain the data illustrated in Figure 5, first the gray scale of the edge function f(x)+B using a Haar-Gauss wavelet with an arbitrary bandwidth to obtain an approximate midpoint (with maximum slope) of the edge curve should convert.

After calculating the slope at this point k_0 and setting β, the wavelet bandwidth from equation (19) can be chosen. Then, the gray edge curve is transformed again using the H-G wavelet with the selected bandwidth. The zero point now indicates the exact edge location. Since the bandwidths of the H-G wavelet follow the bandwidths of the edge function, similar accuracies is obtained for different defocusing conditions.

The maximum error is small (0.22%) and the average error is also small (0.075 %). This means that correct results can be obtained at large defocusing distances and that the edge of a large object can be detected with high accuracy.

Single edge detection was carried out using the integral transform with Haar-Gauss wavelet in the domain of x space and frequency ν. Since the proposed Haar-Gauss wavelet transform at q=s is similar to a wavelet transform with a "Mexican hat" wavelet, this suggests that a function of "Mexican hat" type can also be used in the same procedure.

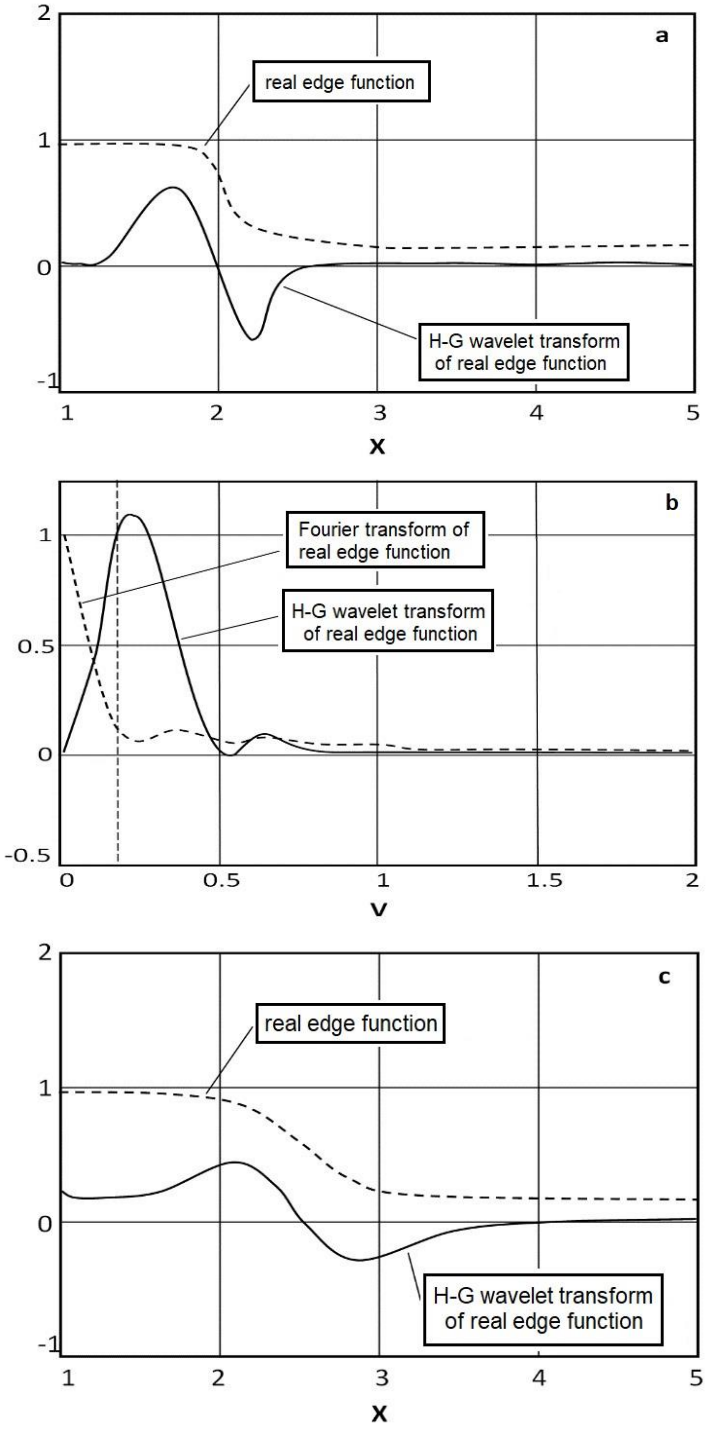
a
real edge function
H-G wavelet transform
of real edge function
2
1
0
-1
1
2
3
4
5
X
b
Fourier transform of
real edge function
H-G wavelet transform
of real edge function
1
0.5
0
-0.5
0
0.5
1
1.5
2
V
c
real edge function
H-G wavelet transform
of real edge function
2
1
0
-1
1
2
3
4
5
X

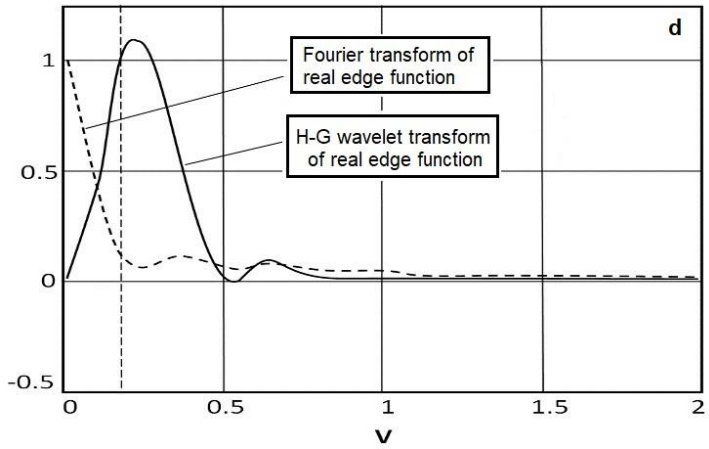

Fig. 5. The Haar-Gauss wavelet transform of real edge f(x) and its Fourier spectrum H(ν) for small (a, b) and large (c, d) edge width (D=Δ)

For double edge detection (Fig. 6), a Haar-Gauss integral wavelet transform with double peaks can also be used, which can detect edges in one step by setting the distance between two peaks. In Figure 6 the double edge intensity function (solid line) and its corresponding Haar-Gauss wavelet transform was simulated.

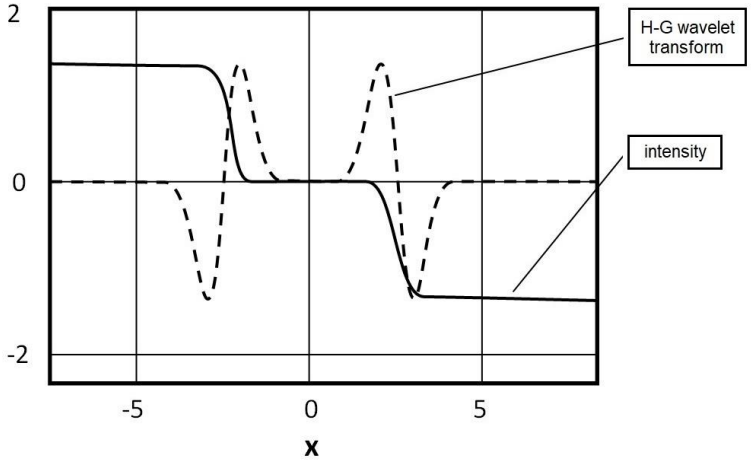

Fig. 6. Double edge intensity function (solid line) and its Haar-Gauss integral wavelet transform (broken line)

CONCLUSIONS

A mathematical model of a non-sharp edge and a bandwidth matching algorithm have been proposed such that the H-G wavelet bandwidth follows the edge frequency bandwidth in order to obtain a large depth of field, high detection precision and fast numerical calculations. The proposed Haar-Gauss wavelet transform and the wavelet bandwidth matching algorithm can be an important tool for edge detection in transport vision systems with large depth of field.

ABBREVIATIONS

1. **DOF** – depth of field;
2. **H-G** – Haar-Gauss wavelet transform;
3. **UF** – uncerta intyfactor.

METODA FALKOWA DETEKCJI KRAWĘDZI W OBRAZACH O WYSOKIM POZIOMIE SZUMÓW

W artykule zaproponowano model matematyczny nieostrej krawędzi oraz całkową transformatę z falka Haara-Gaussa wraz z algorytmem dopasowania pasma zarówno w przestrzeni x jak i w dziedzinie częstotliwości. Zilustrowano

detekcję pojedynczej i podwójnej krawędzi wykorzystując całkową transformatę Haara-Gaussa. Proponowany model krawędzi wraz z transformatą falkową i algorytmem dopasowania szerokości pasma częstotliwości falki może być ważnym narzędziem w rozpoznawaniu obiektów przez nowoczesne wizyjne systemy transportowe.

Słowa kluczowe: transformata falkowa, detekcja krawędzi, cechy charakterystyczne, falka Haara-Gaussa

REFERENCES

[1] Mallat S. (1999) A wavelet tour of signal processing, Academic Press, San Diego, CA, ISBN 9780124666061
[2] Meyer Y. (1993) Wavelets: Algorithms and Applications, Society for Industrial and Applied Mathematics, Philadelphia, ISBN 0898713099
[3] Białasiewicz J. (2000) Falki i aproksymacje, Wydawnictwo Naukowo-Techniczne, Warszawa, ISBN 8320425573
[4] Ziółko M. (2000) Modelowanie zjawisk falowych, AGH, Uczelniane Wydawnictwa Naukowo - Dydaktyczne, Kraków, ISBN 8388408550
[5] Niedziela T., Stankiewicz A., Świętochowski M. (2000) "Homographic wavelet analysis in identification of characteristic image features", Optica Applicata, Vol 30, Issue 2-3, ISSN 0078-5466, pp. 349-359
[6] Niedziela T. (2014) "Falkowa kompresja obrazów kolorowych", Logistyka, Vol. 4, full text on CD, ISSN 1231-5478, pp. 2280-2290
[7] Niedziela T. (2014) "Metody falkowe analizy sygnałów", Logistyka, Vol. 6, full text on CD3, ISSN 1231-5478, pp. 7788-7796
[8] Niedziela T. (2016) "Falkowy korelator połączonej transformaty Fouriera", Autobusy: technika, eksploatacja, systemy transportowe, Section: Logistics, Vol. 6, full text on CD, ISSN 1509-5878, pp. 1458-1461